Into the Void: Single Nanopore in Colloidally Synthesized Bi_2Te_3 Nanoplates with Ultralow Lattice Thermal Conductivity

Tanner Q. Kimberly[1], Evan Y. C. Wang[1], Gustavo D. Navarro[1], Xiao Qi[2], Kamil M. Ciesielski[3], Eric S. Toberer[3] and Susan M. Kauzlarich[1]*

[1]Department of Chemistry, University of California, One Shields Avenue, Davis, California 95616, United States

[2]The Molecular Foundry, Lawrence Berkeley National Lab, Berkeley, California 94720, United States

[3]Department of Physics, Colorado School of Mines, 1523 Illinois Street, Golden, Colorado 80401, United States

Corresponding author email: smkauzlarich@ucdavis.edu

Abstract: Bi_2Te_3 is a well-known thermoelectric material that was first investigated in the 1960s, optimized over decades, and is now one of the highest performing room-temperature thermoelectric materials to-date. Herein, we report on the colloidal synthesis, growth mechanism, and thermoelectric properties of Bi_2Te_3 nanoplates with a single nanopore in the center. Analysis of the reaction products during the colloidal synthesis reveals that the reaction progresses via a two-step nucleation and epitaxial growth: first of elemental Te nanorods, then the binary Bi_2Te_3 nanoplate growth. The rates of epitaxial growth can be controlled during the reaction, thus allowing the formation of a single nanopore in the center of the Bi_2Te_3 nanoplates. The size of the nanopore can be controlled by changing the pH of the reaction solution; where larger pores with diameter of ~50 nm are formed at higher pH and smaller pores with diameter of ~16 nm are formed at lower pH. We propose that the formation of the single nanopore is mediated by the Kirkendall effect and thus the reaction conditions allow for the selective control over pore size. Nanoplates have well defined hexagonal facets as seen in the scanning and transmission electron microscopy images. The single nanopores have a thin amorphous layer at the edge, revealed by transmission electron microscopy. Thermoelectric properties of the pristine and single-nanopore Bi_2Te_3 nanoplates were measured in the parallel and perpendicular directions. These properties reveal strong anisotropy with a significant reduction to thermal conductivity and increased electrical resistivity in the perpendicular direction due to the higher number of nanoplate and nanopore interfaces. Furthermore, Bi_2Te_3 nanoplates with a single nanopore exhibit ultralow lattice thermal conductivity values, reaching ~ 0.21 $Wm^{-1}K^{-1}$ in the perpendicular direction. The lattice thermal conductivity was found to be

systematically lowered with pore size, allowing for the realization of a thermoelectric figure of merit, zT of 0.75 at 425 K for the largest pore size.

---

1. Introduction

The rising energy demands and environmental concerns of the 21st century require new methods of clean power generation with high efficiency, where thermoelectric materials can satisfy these criteria.[1] The design and implementation of efficient thermoelectric materials is often a challenging feat due to the interconnected nature of the thermoelectric properties.[2] Many strategies have been utilized to boost the thermoelectric performance of such materials, including doping,[3] alloying,[4] and creating composites.[5,6] The thermoelectric performance of a material is described by the equation $zT = S^2T/\rho\kappa$, where ρ is electrical resistivity, S, the Seebeck coefficient, and κ is thermal conductivity. However, while the aforementioned strategies will enhance one or more thermoelectric properties, namely the electrical resistivity, Seebeck coefficient, or thermal conductivity, they are often deleterious to the other properties. The carrier concentration of the material largely dictates the thermoelectric properties; thus, doping or alloying has limitations on the enhancement of thermoelectric performance.[7–11] Although, there have been recent examples where these interrelated properties have been decoupled, through interstitial doping or creating vacancies in specific materials.[12–15] Despite these material properties being dependent on carrier concentration, the thermal conductivity can be decoupled into electronic (κ_e) and lattice (κ_L) components, where $\kappa = \kappa_e + \kappa_L$. One method that has proven successful in decoupling these interwoven properties is nanostructuring, which has allowed for the realization of ultralow κ_L.[16]

Many thermoelectric materials have seen zT enhancements from nanostructuring efforts.[17–19] One such material is Bi_2Te_3, which belongs to the family of layered tetradymite structures and can be synthesized with two-dimensional (2D) nanoplate morphology.[20–26] Nanostructured Bi_2Te_3 and its alloys, prepared from bottom-up synthesized nanocrystals or nanograin bulk powders, have proven to be efficient thermoelectric materials, with $zT \geq 1$ at temperatures useful for energy conversion where waste heat is present.[27–29] The large

enhancement of the *zT* in these materials is largely attributed to the significantly lowered thermal conductivity in relation to the bulk counterparts.[30] Ultrathin 2D Bi_2Te_3 nanoplates have thermal conductivity values of ~ 0.4 $Wm^{-1}K^{-1}$, when synthesized as one to three quintuple layers.[31] Core-shell Bi_2Te_3/Sb_2Te_3 nanoplates have been shown to have comparable thermal conductivity values.[32] Alloy nanoplates of $Bi_{2-x}Sb_xTe_3$ with κ_L values as low as 0.29 $Wm^{-1}K^{-1}$ have also been reported.[28]

Recently there has been growing interest in nanoporous materials,[33–35] in particular for thermoelectric applications.[36,37] Tang and coworkers reported on holey silicon, which was prepared via lithographic techniques, and shown to have good thermoelectric performance due to the extraordinary reduction in thermal conductivity, reaching values of ~ 1.76 $Wm^{-1}K^{-1}$, which is more than an order of magnitude lower than the non-porous analog.[38] Porous structures of Ag_2Se[39] and Bi_2Te_3,[40] which were obtained under various sintering conditions, have also been reported to have significantly lowered thermal conductivities. Ordered nanoporous structures of Bi_2Te_3 with tunable porosity have been successfully synthesized via physical vapor deposition techniques.[41] While advancements in nanoporous thermoelectric materials have proven fruitful, many of the synthetic methods that are utilized are often elaborate or offer little control over pore size and morphology.

One very promising synthetic approach to porous and hollow nanostructures is colloidal solution synthesis. Hollow nanostructured alloys of $Bi_2Se_{3-x}Te_x$ that were synthesized from a large-scale solution process have been reported and show a high degree of porosity with ultralow κ_L values.[42] Furthermore, there have been reports of 2D Bi_2Te_3 nanoplates synthesized with a single nanopore in the center.[43,44] Although the synthesis of these nanoporous structures has been observed, the mechanism of formation has proven elusive. Moreover, the thermoelectric properties of single-nanopore Bi_2Te_3 nanoplates have not been explored to the best of our knowledge.

We have previously reported on the synthesis and thermoelectric properties of pristine Bi_2Te_3 and Sb_2Te_3 nanoplates and have shown enhancement of *zT* with nanostructuring.[6] Herein, we report the synthesis, growth mechanism, and thermoelectric properties of hexagonal 2D Bi_2Te_3 nanoplates with a single nanopore in the center. The nanoplates were

characterized by powder x-ray diffraction (PXRD), transmission electron microscopy (TEM), and scanning electron microscopy coupled with energy dispersive x-ray spectroscopy (SEM/EDX). The nanopore size ranges from 16 nm up to 50 nm by varying the concentration of the reducing agent in the solution. We carried out ex-situ studies of the reaction dynamics as a function of time, where we characterized the reaction products every hour via SEM/EDX, in order to propose a mechanism of formation. Finally, the thermoelectric properties were investigated as a function of nanopore morphology and measurement direction, revealing ultralow κ_L and enhanced thermoelectric performance.

2. Experimental

2.1 Synthesis of Nanoplates

Colloidal synthesis of the Bi_2Te_3 nanoplates was accomplished by stirring 5.821 g $Bi(NO_3)_3 \bullet 5H_2O$ (Alfa Aesar, 98%), 3.990 g Na_2TeO_3 (Sigma Aldrich, 99%), and 4.000 g polyvinylpyrrolidone (PVP) (Sigma Aldrich, ~40,000 MW) in 200 mL of a sodium hydroxide (Fisher Scientific) and ethylene glycol (Sigma Aldrich, 99%) solution. The concentration of sodium hydroxide in solution was varied from 0.375 M to 0.500 M. The sodium hydroxide in ethylene glycol solution was dried over 3 Å molecular sieves, at ~10 volume %, for at least 24 hours prior to use. The reaction mixture was degassed and purged with argon gas three times. The reaction solution was heated to 100°C for ~ 30 minutes until all precursors were dissolved, at which point the solution was a pale yellow color. The reaction was done in a 1L three-neck round bottom flask equipped with a heating mantle and condenser at 185°C for 6 hours under argon gas flow. Temperature was controlled with a thermocouple placed directly into the reaction solution. After heating, the reaction solution was allowed to cool to room temperature naturally and then evenly aliquoted into eight 50 mL centrifuge tubes. Subsequently, 25 mL of acetone was added to each solution. The nanoplates were subjected to centrifugation at 8500 rpm for 5 minutes. The dark supernatant was discarded, and the pellet was redispersed in 30 mL of ethanol. The nanoplates were washed three more times with ethanol.

The nanoplates are dispersed in 30 mL of water, further washed three more times and then dispersed into ethanol. Once isolated, the nanoplates were recovered by centrifugation and

dried for two hours under vacuum to remove the residual solvent. The pellet was annealed for 1 hour at 300 °C in an alumina ceramic crucible boat in a tube furnace under argon gas flow to thoroughly remove any remaining surfactant, as previously described by Liu, et. al.[45] The dried pellet was ground with an agate mortar and pestle, and the powder was sieved. The products obtained from both single-pore Bi_2Te_3 nanoplate reactions had a yield of ~90%, (~4.3 g).

2.2 Characterization of Nanoplates

The nanoplates were analyzed by powder x-ray diffraction (PXRD) on a Bruker D8 Advance diffractometer using Cu Kα radiation operated at 40 kV and 25 mA at room temperature. The size and morphology of the nanoplates were assessed using a Thermo Fisher Quattro S Environmental and/or FEI Scios Dual Beam scanning electron microscope (SEM) operated at 15 kV. Compositional analysis was obtained using an Oxford X-Max Energy Dispersive X-ray Spectroscopy (EDX) detector equipped to the FEI Scios Dual Beam SEM. TEM and High-resolution TEM (HRTEM) were acquired using a FEI ThemIS 60−300 STEM/TEM (Thermo Fisher Scientific, US) operated at 300 kV at the National Center for Electron Microscopy within the Molecular Foundry in Lawrence Berkeley National Laboratory. The ThemIS is equipped with image aberration corrector optics, and a Ceta2 camera (4k × 4k pixels, and 14-bit dynamic range).

2.3 Spark Plasma Sintering

The thermoelectric properties were measured on the consolidated powder in the form of a pellet, prepared using a Dr. Sinter Junior Spark Plasma Sintering SPS-2ll LX system (Fuji Electronic Industrial Co., LTD) under vacuum. The nanoplate powders (~3-4 g) were loaded into a 10 mm graphite die with graphite plungers and 16 pieces of graphite foil on each side to ensure air-free conditions. The 10 mm die was inserted into a larger 20 mm die with graphite plungers and 6 graphite foils on each side, with a thermocouple placed into a hole drilled into the 20 mm die to ensure precise temperature control. The nanoplate powder was initially cold pressed at 45 MPa for 3 min under static vacuum. After the cold press, the holding pressure was increased to 89 MPa over 5 min and held for the remaining 10 min, while the die was

simultaneously heated from room temperature to 370 °C over 3 min and then to 400 °C over 1 min and held at 400 °C for 11 min. The die was naturally cooled after the SPS process and a ~7 mm thick gray/metallic pellet was obtained. The pellet was cut in two directions, parallel and perpendicular to the SPS direction, and polished to obtain one 10 mm diameter by 1 mm thick circular pellet and a 6 mm^2 by 1 mm thick square pellet. The circular and square pellets were also analyzed by SEM to obtain information about the preferred orientation and texturing of the nanoplate pellet.

2.4 Thermoelectric Property Measurements

Thermal diffusivity of the sample was measured using a Netzsch Laser Flash Analysis (LFA) instrument, from which κ was calculated, using the equation $\kappa(T) = \rho C_p \alpha(T)$. Where ρ is the density, C_p is the heat capacity, and $\alpha(T)$ is the thermal diffusivity. Thermal diffusivity measurements were done with a heating and cooling cycle with 25 K increments in the range of 300 to 500 K. Electronic measurements were carried out on the sample to determine carrier transport. Temperature dependent Seebeck coefficient, S, was measured from 300 to 500 K on a custom-built apparatus using 300 Torr of nitrogen atmosphere to ensure proper thermal contact between the sample and the heating blocks.[46] The Hall effect and resistivity were measured with Van der Pauw technique on a custom-built apparatus; the experiments were performed between 300 and 500 K under dynamic vacuum.[47] Heating and cooling cycles were done on all electronic transport measurements to ensure that samples do not evolve with temperature cycling.

3. Results and Discussion

3.1 Nanoplate Structure and Morphology Analysis

During the synthesis of pristine Bi_2Te_3 nanoplates by the method previously published in our group,[6] we found that some reactions yielded nanoplates with a single nanopore, typically when the solution was not rigorously dried over molecular sieves (Supporting Information (SI), Figure S1). We hypothesized that the reducing ability of the solvent impacted the size of the pore, and thus utilized the basicity of the solvent as a tunability parameter in the nanopore

synthesis. Both reactions, carried out with [NaOH] = 0.375 M and 0.500 M, yielded phase pure Bi_2Te_3 as shown in the PXRD pattern of Figure 1a. By further inspection with TEM analysis, shown in Figures 1b and 1c, the products consisted of nanoplates with smaller nanopores and larger nanopores, respectively.

Bi_2Te_3 nanoplates with small nanopores were formed from the reaction with [NaOH] = 0.375 M and large nanopores were formed with [NaOH] = 0.500 M. Both the small and large single-pore nanoplates exhibit 2D hexagonal morphology. The Bi_2Te_3 single-pore nanoplates range approximately from 0.5 µm to 1 µm in their lateral dimension. By TEM and SEM analysis (SI, Figures S2 and S3), the small pores are ~ 16 nm and the large pores are ~ 50 nm in diameter, on average. With these data in hand, we conclude that by varying the concentration of NaOH, which acts as the auxiliary reducing agent in this polyol synthesis,[48] two nanopore size regimes are observed in the single-nanopore nanoplates. These reactions were each carried out in triplicate to ensure reproducibility (SI, Figures S4 and S5), and each time yielded small and large nanopores, with [NaOH] = 0.375 M and 0.500 M, respectively.

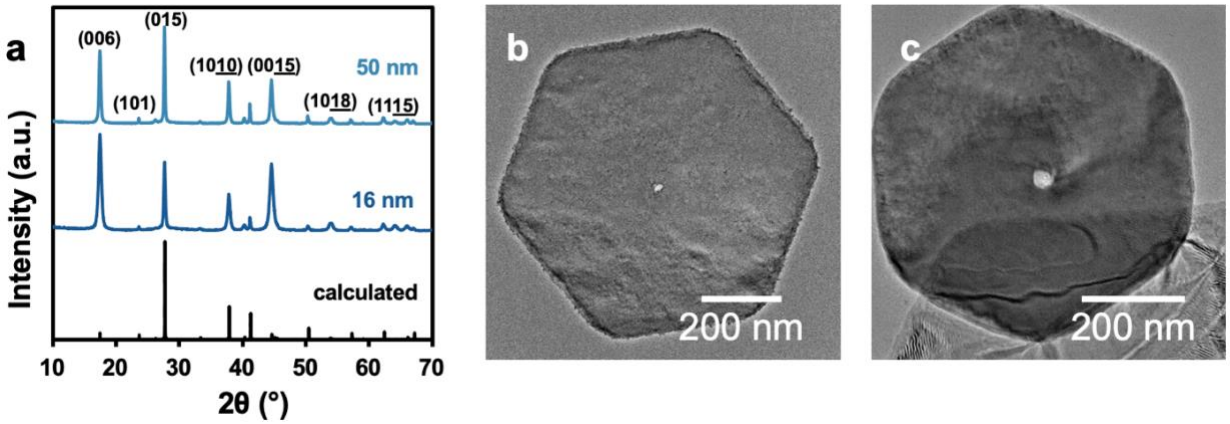

Figure 1. PXRD pattern (a) and TEM micrograph of Bi_2Te_3 nanoplates with (b) small pore and (c) large pore.

3.2 Growth Mechanism of Bi_2Te_3 Nanoplates with Single Nanopore

In order to investigate the mechanism of formation for the Bi_2Te_3 nanoplates with a single nanopore, an ex-situ reaction study was carried out in which aliquots of the reaction solution were taken at various time points. The reaction products were analyzed at 1 h, 2 h, 3 h,

4 h, 5 h, and 6 h. The SEM micrographs of reaction products at these time points can be seen in Figure 2.

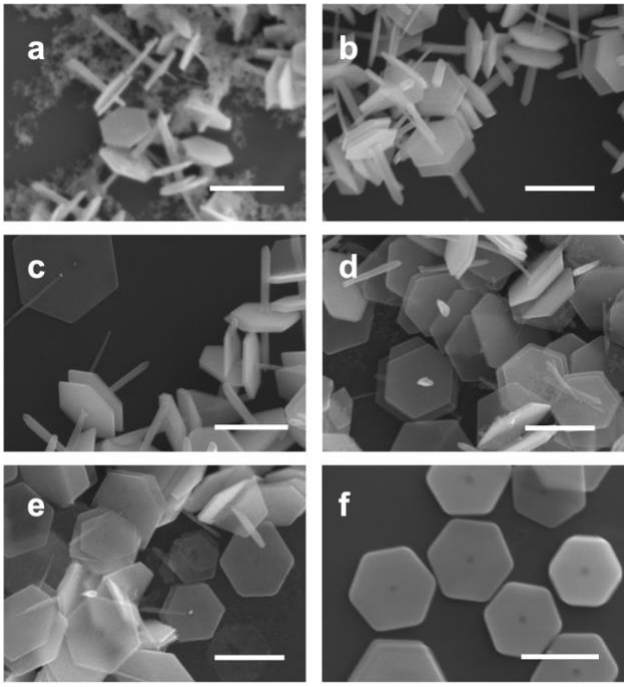

Figure 2. Reaction products of Bi_2Te_3 nanoplate reaction with [NaOH] = 0.500 M. Shown at (a) 1 h, (b) 2 h, (c) 3 h, (d) 4 h, (e) 5 h, (f) 6h. All scale bars are 1 μm.

As seen in the SEM micrographs of the reaction products of the [NaOH] = 0.500 M reaction in Figure 2, there is nucleation and growth of an interpenetrating Te nanorod and Bi_2Te_3 nanoplate structure within the first hour (Figure 2a). These "T-shaped" Te nanorod and Bi_2Te_3 nanoplate heterostructures have been previously reported by Cheng and coworkers, although synthesized using much lower NaOH concentrations.[49] This result is consistent with the lower reducing power of the solvent at lower NaOH concentrations. Other interpenetrating nanorod with nanoplate morphologies have been observed in Bi_2Te_3, $Bi_2Se_{3-x}Te_x$, and $Bi_{2-x}Sb_xTe_3$ materials.[50–52] As the reaction progresses, the Te nanorod is consumed, and the Bi_2Te_3 nanoplate grows epitaxially, as seen at 2 h (Figure 2b), 3 h (Figure 2c), and 4 h (Figure 2d). At 5 h, most of the Te nanorods have detached from the plates, leaving some with a pore and some still containing a Te rich core (Figure 2e). Finally, at 6 h, the Bi_2Te_3 nanoplate pore ripens and

has a distinct morphology. We attribute the evolution from interpenetrating Te nanorod/ Bi_2Te_3 nanoplate to the single-nanopore nanoplate to the Kirkendall effect, where the Te atoms become reduced to Te^{2-} anions and diffuse out at a faster rate than the Bi_2Te_3 grows inward. This effect has been reported to drive the growth of many hollow nanostructures, including metals, chalcogenides and oxides.[53,54] We propose that the reduction rate can be enhanced by increasing the concentration of the auxiliary reducing agent, NaOH, in solution. By increasing the NaOH concentration, the reduction rate of Te is increased, and thus leaves a hole in the center of the nanoplate where the Te nanorod previously occupied.

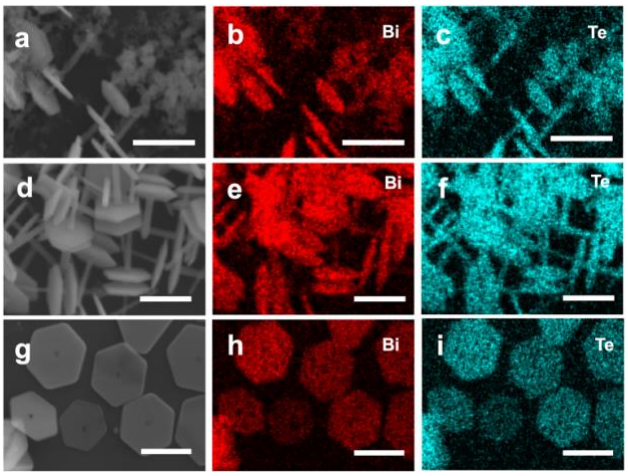

Figure 3. Reaction products of Bi_2Te_3 nanoplate colloidal synthesis using [NaOH] = 0.500 M. (a) SEM image, (b) Bi elemental distribution, and (c) Te elemental distribution of reaction product at 1 h. (d) SEM image, (e) Bi elemental distribution, and (f) Te elemental distribution of reaction product at 2 h. (g) SEM image, (h) Bi elemental distribution, and (i) Te elemental distribution of reaction product at 6 h. All scale bars are 1 µm.

In order to confirm the chemical nature and composition of the reaction intermediates, SEM/EDX mapping was also done on the ex-situ aliquot samples. Figure 3 shows the SEM micrographs of reaction products at 1 h (Figure 3a), 2 h (Figure 3d) and 6 h (Figure 3g). The EDX maps of Bi and Te are shown in Figure 3b and Figure 3c for the 1 h product, where the nanorod can be resolved as only Te in composition, and the 2D nanoplate grown around it consist of Bi and Te. At 2 h, the nanorod is still mostly Te, but now has some incorporation of Bi, as shown in

the EDX map of Figure 3e and Figure 3f. The 6 h product is only comprised of Bi_2Te_3 2D nanoplates with a single nanopore as seen in the EDX maps of Figure 3h and Figure 3i.

From our ex-situ SEM/EDX reaction studies, we propose a general reaction mechanism as shown in Figure 4. Starting with the Bi^{3+} and Te^{4+} precursors, we propose there is nucleation and growth of Te nanorods, although this is not observed within the first hour of our reaction as the kinetics are very fast. However, the growth of Te nanorods is observed in the first 30 minutes of Sb_2Te_3 nanoplates, which have slower kinetics, under similar reaction conditions.[55] In the second step, Bi_2Te_3 nanoparticles nucleate onto the Te nanorod. In step three, the Bi_2Te_3 plate begins to epitaxially form around the Te nanorod. In step four, the rod detaches from the plate as it is consumed to form Bi_2Te_3. In step five, the Te atoms are reduced and undergo growth into the Bi_2Te_3 nanoplate, leaving a Kirkendall void, or nanopore.

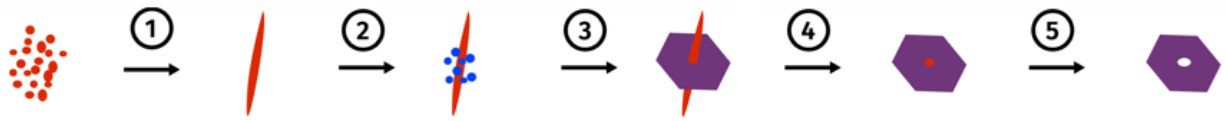

Figure 4. Proposed reaction mechanism of Bi_2Te_3 nanoplates with a single nanopore. Step one is nucleation and growth of a Te nanorod; step two is nucleation of Bi_2Te_3 nanoparticles onto the Te nanorod; step three is epitaxial growth of the Bi_2Te_3 nanoplate around the Te nanorod; step four is dissolution of the nanorod from the nanoplate, leaving a Te rich core; step five is complete consumption of Te core, leaving a Kirkendall void, or nanopore. Te nanorod is shown in red, Bi_2Te_3 nanoparticles shown in blue, and Bi_2Te_3 nanoplate shown in purple.

We suggest the nanopore structure is a metastable product which can be trapped with the proper reaction conditions, i.e. with the appropriate NaOH concentration. When [NaOH] is low (0.375 M) the reduction of Te is slow and leads to the formation of small nanopores on the order of 16 nm. When [NaOH] is high (0.500 M), the Te reduction rate is much faster and leads to the formation of large nanopores on the order of 50 nm. It is apparent that other parameters which were not explored in this study, such as temperature and time, could affect the reaction

rate and pore crystallinity, respectively. Thus, our proposed growth mechanism is generalized and may be further elaborated on by changing additional parameters.

The morphology and crystallinity of a typical nanoplate with a large nanopore was investigated by TEM and HRTEM as shown in Figure 5. The Bi_2Te_3 nanoplate with a large nanopore is shown in the low magnification TEM image in Figure 5a, with a HRTEM image of the same nanopore in the inset, which measures 40 nm in diameter. A HRTEM image of the nanopore edge is shown in Figure 5b, where a thin amorphous layer can be seen around the edge of the pore, but further into the bulk of the nanoplate, it becomes highly crystalline with a measured lattice spacing of 0.218 nm for the (11-20) plane. This lattice spacing is in good agreement with the known crystal structure.[56] The fast Fourier Transform (FFT) of the nanopore edge was taken and shows diffuse rings, indicative of an amorphous region (SI, FigureS6). The presence of a thin amorphous layer suggests that the porous nanoplate is a metastable product, which is trapped during the fast reduction of elemental Te from the heterojunction interface and does not allow the Bi_2Te_3 sufficient time to crystallize around the nanopore edge.

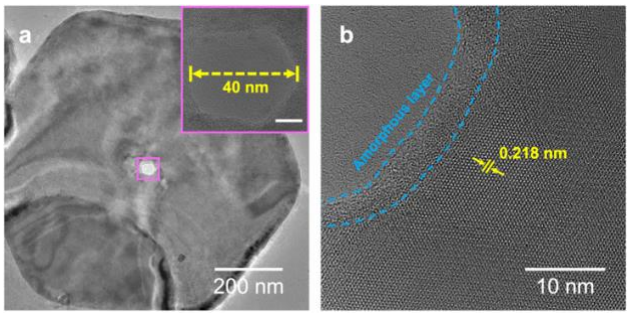

Figure 5. Typical Bi_2Te_3 nanoplate with large nanopore. (a) Low magnification TEM image of nanoplate with HRTEM image of nanopore, shown in the inset (scale bar is 10 nm), with diameter of ~ 40 nm. (b) HRTEM image of edge of the pore with a lattice spacing of 0.218 nm corresponding to the (11-20) plane.

3.3 Characterization of Consolidated Nanoplates with a Single Nanopore

Due to the anisotropy of the layered and Bi_2Te_3 crystal structures, thermoelectric properties are also anisotropic. In order to elucidate the anisotropy in thermoelectric performance of the nanoplates, the consolidated nanoplate pellets are cut in two different

directions denoted “parallel” and “perpendicular”. In the parallel direction, the thermoelectric property measurements are performed parallel to the nanoplate plane. In the perpendicular direction, thermoelectric properties are measured perpendicular to the nanoplate plane. All pellets ranged from 88% to 94% of the theoretical density, determined by the Archimedes principle (SI, Table S1). The pellet densities are relatively low compared to that of the bulk materials due to the retention of nanoplate interfaces, which is achieved by incompletely sintering the nanoplates with a low SPS temperature of 400 °C.

The nanoplate pellets were fractured and analyzed by SEM to obtain information about the microstructure. SEM micrographs of the consolidated single-pore nanoplate pellets are shown in Figure 6. Figure 6a shows the parallel direction and Figure 6b shows the perpendicular direction of the 16 nm nanopore pellet. The parallel and perpendicular direction for the 50 nm nanopore pellet can be seen in Figure 6c and 6d, respectively. A laminar morphology is observed in the parallel direction for both nanopore pellets, in which all nanoplates align with a high degree of preferred orientation. In the perpendicular direction, some of the hexagonal nanoplate morphology, as well as the nanopore morphology, is still maintained as shown in the insets of Figures 6b and 6d. The size of the nanopores do not change significantly during the sintering process, due to the fact that the SPS temperature is well below the melting point of the material. The SEM microscopy analysis confirms that there is strong anisotropy, as well as retention of single nanopores within the consolidated materials, which yields a hierarchical nanostructure.

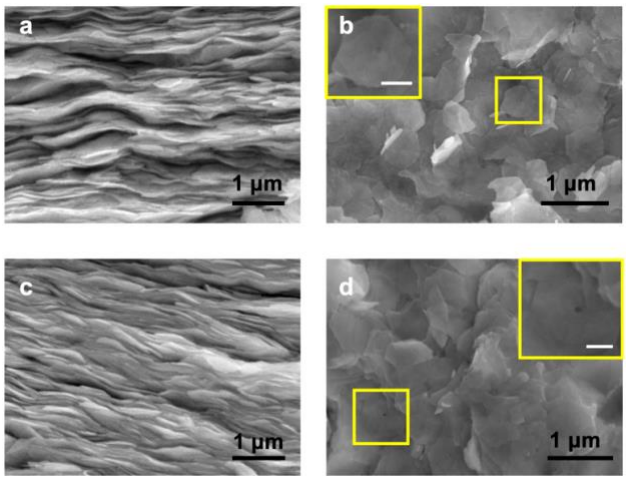

Figure 6. SEM images of the fractured 16 nm nanopore pellet in (a) parallel and (b) perpendicular directions and of the fractured 50 nm nanopore nanoplate pellet in (c) parallel and (d) perpendicular directions. The nanopore morphology is retained in both nanoplate pellets as can be observed in the inset images in the perpendicular directions (inset scale bars are 200 nm).

3.4 Thermoelectric Properties

The thermoelectric properties were measured for the single-pore Bi_2Te_3 nanoplate pellets with 16 nm and 50 nm pore sizes. The thermoelectric properties of the 16 nm and 50 nm single-pore nanoplate pellets were compared to those of the pristine Bi_2Te_3 nanoplate pellets (with no pore). Pristine nanoplates were prepared as described in our previous study, which in short, require shorter reaction time so the core does not undergo prolonged diffusion.[6] This means that time is an additional parameter that can be used to further increase the nanopore size. Thermoelectric properties were measured in both parallel and perpendicular directions to elucidate their anisotropy and the effect of the 2D nature of the plates and the nanopore.

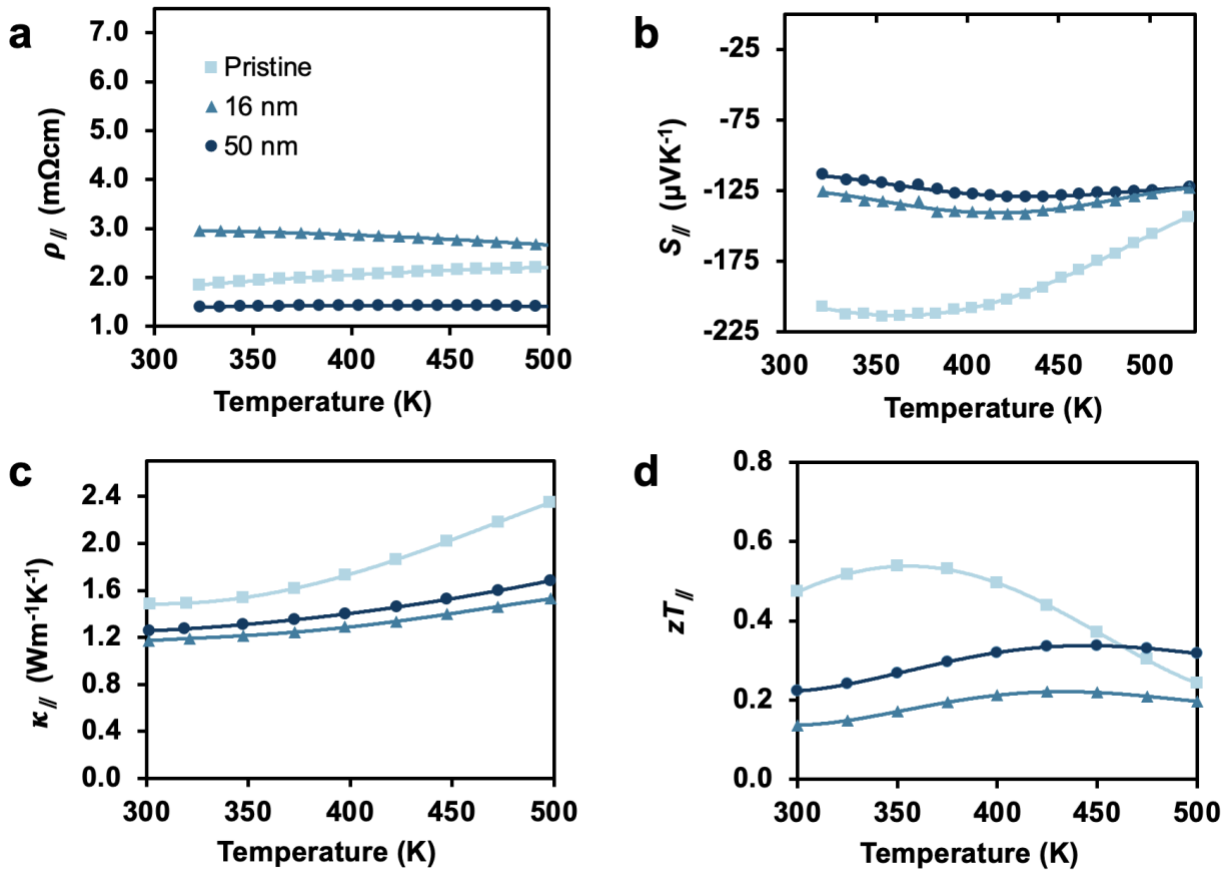

Figure 7. Thermoelectric properties in the parallel direction for Bi_2Te_3 nanoplates with a single nanopore. (a) electrical resistivity, (b) Seebeck coefficient, (c) thermal conductivity, and (d) thermoelectric figure of merit, *zT*.

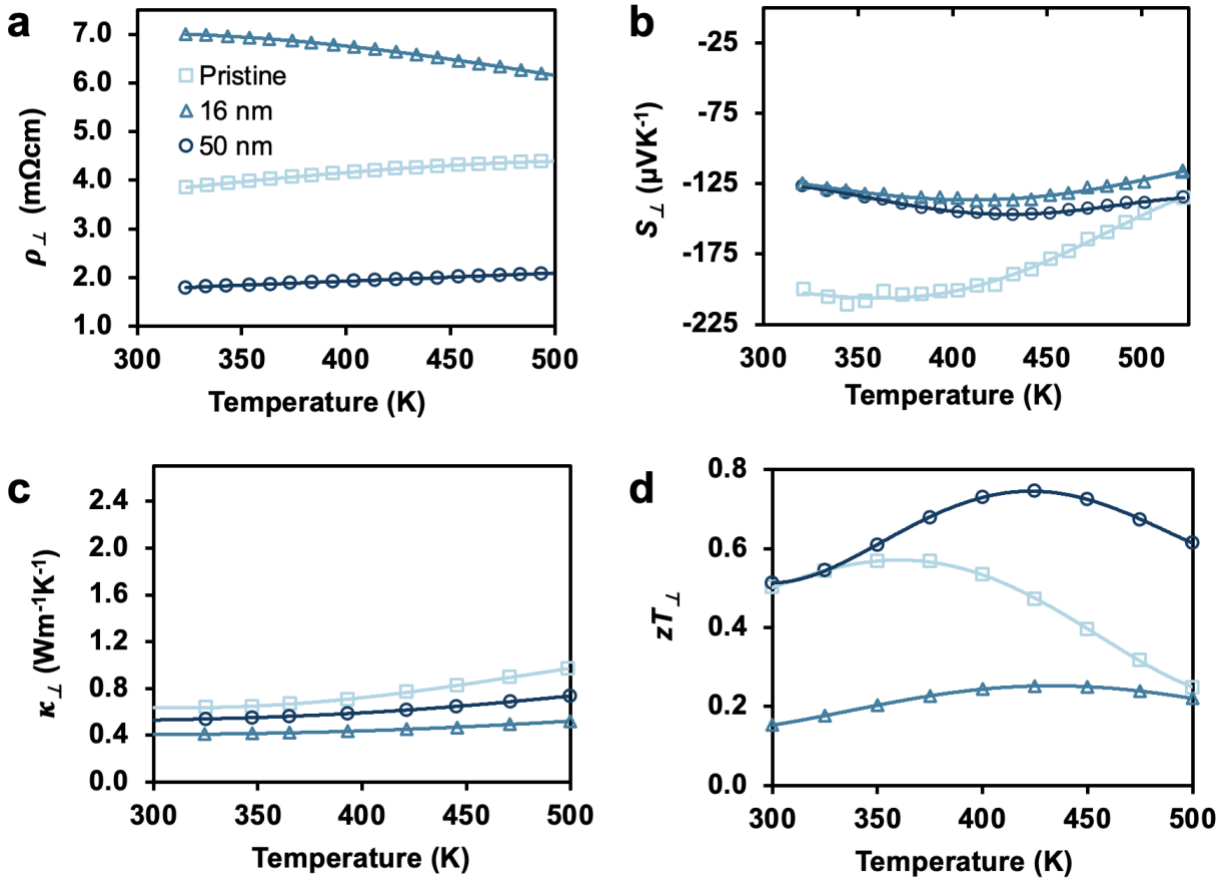

Figure 8. Thermoelectric properties in the perpendicular direction for Bi_2Te_3 nanoplates with a single nanopore. (a) electrical resistivity, (b) Seebeck coefficient, (c) thermal conductivity, and (d) thermoelectric figure of merit, *zT*.

The electrical resistivity is shown in Figures 7a and 8a, which have much higher values in the perpendicular direction compared to the parallel direction due to more interface scattering at the nanoplate planes, as well as the nanopores. We can observe the effect of interface scattering at the nanopore in the Hall mobility data (SI, Figure S7), where the carrier mobility is highest for the pristine sample and is drastically reduced for both size pores in parallel and perpendicular directions. The carrier concentration (SI, Figure S8) shows a gradual increase with pore size, which may indicate greater defect densities, consistent with Bi_2Te_3 to antisite defects, or may be due to the increasing amorphous region around the nanopore edge.[27,57] The electrical resistivity is highest for the 16 nm nanopore nanoplates, followed by the pristine

nanoplates, and the lowest being the 50 nm nanopore nanoplates. The high electrical resistivity in the 16 nm nanoplates is due to a combination of charge carrier scattering at the nanopore, as well as the relatively low carrier concentration. The lowest electrical resistivity is achieved in the 50 nm nanopore nanoplates due to their very high carrier concentration. There is no hysteresis in the electrical resistivity data upon heating and cooling cycles (SI, Figure S9).

The Seebeck coefficients, shown in Figures 7b and 8b, are negative, which indicates that the materials are n-type. This carrier type is consistent with previously reported defects in this system, which lead to n-type behavior.[58] The values are roughly equivalent in both the parallel and perpendicular directions. However, the nanoplates with both a 16 nm and 50 nm nanopore have a much lower Seebeck coefficients than the pristine, reaching values of ~ 150 μVK^{-1}. This effect could be due to the different carrier concentration, or changes to the carrier effective mass as the nanoplate morphology is altered. Although the Seebeck starts very negative at ~210 μVK^{-1} in the pristine sample, it begins to increase to less negative values, likely due to the onset of bipolar conduction, and the low amount of majority carriers. The Seebeck data does not show any hysteresis upon heating and cooling cycles (SI, Figure S9). In order to better understand the electronic contribution to the figure of merit, the power factor (σS^2) was calculated for all nanoplates in both parallel and perpendicular directions, which displays a maximum of ~ 11 $Wm^{-1}K^{-1}$ for the 50 nm pore nanoplates (SI, Figure S10).

The thermal conductivity of the Bi_2Te_3 nanoplates is very low in the parallel direction (Figure 7c), and is decreased even further in the perpendicular direction, with values ranging from ~ 0.4 to 1.0 $Wm^{-1}K^{-1}$ (Figure 8c). This reduction in thermal conductivity is again due to the large number of nanoplate interfaces, leading to more phonon scattering. Moreover, the thermal conductivity is further reduced with the introduction of nanopores. The lattice thermal conductivity was calculated, according to $\kappa_L = \kappa - \kappa_e$, where $\kappa_e = LT/\rho$, and is shown in Figure 9a and 9b, for the parallel and perpendicular directions, respectively. The κ_L monotonically decreases as the size of the nanopore is increased. We believe κ_L is monotonically lowered as pore size is increased due to acoustic phonon scattering which is primarily responsible for transporting heat.[59] Larger pore sizes will interact with longer wavelength (acoustic) phonons whereas a small pore will only interact with short wavelength

(optical) phonons. Additionally, we hypothesize that the amorphous region near the nanopore edge affects the thermoelectric properties, since it adds additional disorder in the system, which may contribute to further reduction of κ_L. The lowest κ_L values are for the 50 nm nanopore pellet, reaching a value of ~ 0.21 $Wm^{-1}K^{-1}$ in the perpendicular direction. These ultralow thermal conductivity values are due to the increased phonon scattering at the nanopore and can be tuned with controlling the nanoscale void size. The thermal conductivity data is fit excellently upon heating and cooling cycles.

The *zT* values in the parallel direction (Figure 7d) are higher for the pristine nanoplates than for the nanoplates with a single nanopore, reaching a maximum value of 0.53. This is likely due to the large Seebeck coefficient in the pristine nanoplates and the moderately low thermal conductivity and electrical resistivity. However, the *zT* values in the perpendicular direction (Figure 8d) are much higher for the nanoplates with a 50 nm nanopore. This enhanced *zT* is largely due to the ultralow κ_L in the single-nanopore pellet. A maximum *zT* of 0.75 is achieved in the perpendicular direction for the nanoplates with a 50 nm nanopore, which is evidence that suggests nanoscale void engineering is a reliable strategy to enhance the thermoelectric performance of many materials. Although this is not an extremely high *zT* that would be competitive with current state-of-the-art thermoelectrics, the electronic properties may be tuned by doping/alloying these single-nanopore materials to enhance the Seebeck or electrical conductivity while simultaneously retaining the ultralow κ_L and thus allowing the prospect for greater thermoelectric optimization.

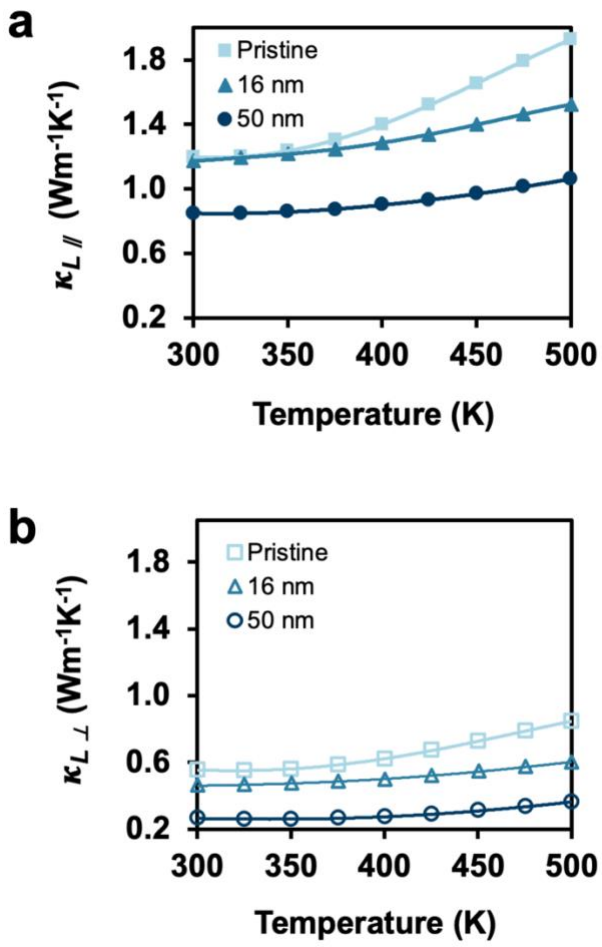

Figure 9. Lattice thermal conductivity of Bi_2Te_3 nanoplates with a single nanopore in the (a) parallel and (b) perpendicular directions.

4. Conclusion

We report the synthesis, characterization, and growth mechanism of 2D hexagonal Bi_2Te_3 nanoplates with and without a single nanopore by varying the auxiliary reducing agent (NaOH) concentration. This synthesis utilizes the colloidal polyol approach and allows for large scale yields of these single-pore nanoplates. Nanopores with a size of ~ 16 nm and ~ 50 nm were obtained at [NaOH] = 0.375 M and 0.500 M, respectively. A typical nanopore was investigated further by TEM and HRTEM, displaying an irregularly shaped pore with a thin amorphous layer at the edge. Through ex-situ reaction studies, the reaction dynamics are elucidated, showing first the formation of Te nanorods, then an interpenetrating

nanorod/nanoplate structure, and finally porous nanoplates. With these investigations, a mechanism of formation is proposed. Finally, the thermoelectric properties of the nanoporous and pristine Bi_2Te_3 nanoplates as a function of measurement direction are reported, showing successful modulation of the lattice thermal conductivity with the introduction of nanopores into 2D Bi_2Te_3 nanoplates. Tailoring of the ultralow lattice thermal conductivity values resulted in a significant enhancement of the thermoelectric performance, reaching a maximum zT of 0.75 in the perpendicular direction at 425 K for the largest nanopores. Doping, alloying, and preparing nanocomposites of these nanoporous Bi_2Te_3 may further enhance the zT. The ability to systematically reduce κ_L as a function of nanoscale void engineering is highly desirable and may lead to revolutions in the next generation of thermoelectric materials.

5. Supporting Information

SEM image of nanoporous Bi_2Te_3 nanoplate product obtained when NaOH and ethylene glycol solution was not dried over molecular sieves; TEM images and histogram of pore size measurements on small nanopore nanoplates; SEM image and histogram of pore size measurements on large nanopore nanoplates; SEM images of small pore nanoplate reaction products carried out in triplicate; SEM images of large pore nanoplate reaction products carried out in triplicate; HRTEM and FFT of nanopore edge; table of densities for all Bi_2Te_3 nanopore nanoplate pellets measured by the Archimedes principle; Hall carrier mobility of single nanopore nanoplates; Hall carrier concentration of single nanopore nanoplates; temperature cycling for Seebeck and electrical resistivity data for all samples; power factor for all samples.

6. Acknowledgements

This work was supported by the National Science Foundation, DMR-2001156, DMR-2307231, and CAREER DMR-1555340. Electron microscopy at the Molecular Foundry was supported by the Office of Science, Office of Basic Energy Sciences, of the U.S. Department of Energy under Contract No. DE-AC02- 05CH11231. The authors are grateful to the Advanced Materials Characterization and Testing Lab (AMCaT) in the UC Davis Department of Materials Science and Engineering for access to the SEM instrumentation. Part of this study was carried out at the UC Davis Center for Nano and Micro Manufacturing (CNM2).

7. References

(1) Ahmad, T.; Zhang, D. A Critical Review of Comparative Global Historical Energy Consumption and Future Demand: The Story Told so Far. *Energy Reports* **2020**, *6*, 1973–1991. https://doi.org/10.1016/j.egyr.2020.07.020.

(2) Snyder, G. J.; Toberer, E. S. Complex Thermoelectric Materials. *Nat. Mater.* **2008**, *7*, 105–114. https://doi.org/10.1038/nmat2090

(3) Mehta, R. J.; Zhang, Y.; Zhu, H.; Parker, D. S.; Belley, M.; Singh, D. J.; Ramprasad, R.; Borca-Tasciuc, T.; Ramanath, G. Seebeck and Figure of Merit Enhancement in Nanostructured Antimony Telluride by Antisite Defect Suppression through Sulfur Doping. *Nano Lett.* **2012**, *12* (9), 4523–4529. https://doi.org/10.1021/nl301639t.

(4) Hu, L. P.; Zhu, T. J.; Yue, X. Q.; Liu, X. H.; Wang, Y. G.; Xu, Z. J.; Zhao, X. B. Enhanced Figure of Merit in Antimony Telluride Thermoelectric Materials by In-Ag Co-Alloying for Mid-Temperature Power Generation. *Acta Mater.* **2015**, *85*, 270–278. https://doi.org/10.1016/j.actamat.2014.11.023.

(5) Wang, X. Y.; Wang, H. J.; Xiang, B.; Fu, L. W.; Zhu, H.; Chai, D.; Zhu, B.; Yu, Y.; Gao, N.; Huang, Z. Y.; Zu, F. Q. Thermoelectric Performance of Sb_2Te_3-Based Alloys Is Improved by Introducing PN Junctions. *ACS Appl. Mater. Interfaces* **2018**, *10* (27), 23277–23284. https://doi.org/10.1021/acsami.8b01719.

(6) Kimberly, T. Q.; Ciesielski, K. M.; Qi, X.; Toberer, E. S.; Kauzlarich, S. M. High Thermoelectric Performance in 2D Sb_2Te_3 and Bi_2Te_3 Nanoplate Composites Enabled by Energy Carrier Filtering and Low Thermal Conductivity. **2024**, 6, (5) 2816-2825. https://doi.org/10.1021/acsaelm.3c00385.

(7) Tan, G.; Zhao, L. D.; Kanatzidis, M. G. Rationally Designing High-Performance Bulk Thermoelectric Materials. *Chem. Rev.* **2016**, *116* (19), 12123–12149. https://doi.org/10.1021/acs.chemrev.6b00255.

(8) Chung, D. Y.; Hogan, T. P.; Rocci-Lane, M.; Brazis, P.; Ireland, J. R.; Kannewurf, C. R.; Bastea, M.; Uher, C.; Kanatzidis, M. G. A New Thermoelectric Material: $CsBi_4Te_6$. *J. Am. Chem. Soc.* **2004**, *126* (20), 6414–6428. https://doi.org/10.1021/ja039885f.

(9) Li, D.; Gong, Y.; Chen, Y.; Lin, J.; Khan, Q.; Zhang, Y.; Li, Y.; Zhang, H.; Xie, H. Recent Progress of Two-Dimensional Thermoelectric Materials. *Nano-Micro Lett.* **2020**, 12, 36. https://doi.org/10.1007/s40820-020-0374-x.

(10) Xiong, F.; Tan, H. Bin; Xia, C.; Chen, Y. Strain and Doping in Two-Dimensional SnTe Nanosheets: Implications for Thermoelectric Conversion. *ACS Appl. Nano Mater.* **2020**, *3* (1), 114–119. https://doi.org/10.1021/acsanm.9b01793.

(11) Hong, M.; Lyu, W.; Wang, Y.; Zou, J.; Chen, Z. G. Establishing the Golden Range of Seebeck Coefficient for Maximizing Thermoelectric Performance. *J. Am. Chem. Soc.* **2020**, *142* (5), 2672–2681. https://doi.org/10.1021/jacs.9b13272.

(12) Wang, D. Z.; Liu, W. Di; Mao, Y.; Li, S.; Yin, L. C.; Wu, H.; Li, M.; Wang, Y.; Shi, X. L.; Yang, X.; Liu, Q.; Chen, Z. G. Decoupling Carrier-Phonon Scattering Boosts the Thermoelectric Performance of n-Type GeTe-Based Materials. *J. Am. Chem. Soc.* **2024**, *146* (2), 1681–1689. https://doi.org/10.1021/jacs.3c12546.

(13) Yu, Y.; Xu, X.; Wang, Y.; Jia, B.; Huang, S.; Qiang, X.; Zhu, B.; Lin, P.; Jiang, B.; Liu, S.; Qi, X.; Pan, K.; Wu, D.; Lu, H.; Bosman, M.; Pennycook, S. J.; Xie, L.; He, J. Tunable Quantum Gaps to Decouple Carrier and Phonon Transport Leading to High-Performance Thermoelectrics. *Nat. Commun.* **2022**, *13* (1). https://doi.org/10.1038/s41467-022-33330-9.

(14) Ge, B.; Lee, H.; Im, J.; Choi, Y.; Kim, S. Y.; Lee, J. Y.; Cho, S. P.; Sung, Y. E.; Choi, K. Y.; Zhou, C.; Shi, Z.; Chung, I. Engineering an Atomic-Level Crystal Lattice and Electronic Band Structure for an Extraordinarily High Average Thermoelectric Figure of Merit in n-Type PbSe. *Energy Environ. Sci.* **2023**, *16* (9), 3994–4008. https://doi.org/10.1039/d3ee01226c.

(15) Su, L.; Wang, D.; Wang, S.; Qin, B.; Wang, Y.; Qin, Y.; Jin, Y.; Chang, C.; Zhao, L. D. High Thermoelectric Performance Realized through Manipulating Layered Phonon-Electron Decoupling. *Science.* **2022**, *375*, 1385–1389. https://doi.org/10.1126/science.abn8997.

(16) Heremans, J. P.; Dresselhaus, M. S.; Bell, L. E.; Morelli, D. T. When Thermoelectrics Reached the Nanoscale. *Nature Nanotech* **2013**, 8, 471–473. https://doi.org/10.1038/nnano.2013.129.

(17) Shi, X. L.; Zou, J.; Chen, Z. G. Advanced Thermoelectric Design: From Materials and

Structures to Devices. *Chem. Rev.* **2020**, *120* (15), 7399–7515. https://doi.org/10.1021/acs.chemrev.0c00026.

(18) Olivares-Robles, M. A.; Badillo-Ruiz, C. A.; Ruiz-Ortega, P. E. A Comprehensive Analysis on Nanostructured Materials in a Thermoelectric Micro-System Based on Geometric Shape, Segmentation Structure and Load Resistance. *Sci. Rep.* **2020**, *10* (1), 1–13. https://doi.org/10.1038/s41598-020-78770-9.

(19) Kobayashi, K.; Takahashi, M.; Moore, S.; Miyata, M.; Sauerschnig, P.; Uzuhashi, J.; Ohta, M.; Ohkubo, T.; Maenosono, S. Electronic and Thermal Transport Properties of Nanostructured Thermoelectric Materials Sintered from Chemically Synthesized Tin Sulfide Nanoparticles and Effects of Ag and Se Doping. *ACS Appl. Energy Mater.* **2024**, 7, 10, 4484–4493. https://doi.org/10.1021/acsaem.4c00487.

(20) Heremans, J. P.; Cava, R. J.; Samarth, N. Tetradymites as Thermoelectrics and Topological Insulators. *Nat. Rev. Mater.* **2017**, *2*, 17049. https://doi.org/10.1038/natrevmats.2017.49.

(21) Kong, D.; Dang, W.; Cha, J. J.; Li, H.; Meister, S.; Peng, H.; Liu, Z.; Cui, Y. Few-Layer Nanoplates of Bi_2Se_3 and Bi_2Te_3 with Highly Tunable Chemical Potential. *Nano Lett.* **2010**, *10* (6), 2245–2250. https://doi.org/10.1021/nl101260j.

(22) Min, Y.; Roh, J. W.; Yang, H.; Park, M.; Kim, S. Il; Hwang, S.; Lee, S. M.; Lee, K. H.; Jeong, U. Surfactant-Free Scalable Synthesis of Bi_2Te_3 and Bi_2Se_3 Nanoflakes and Enhanced Thermoelectric Properties of Their Nanocomposites. *Adv. Mater.* **2013**, *25* (10), 1425–1429. https://doi.org/10.1002/adma.201203764.

(23) Wu, Z.; Mu, E.; Wang, Z.; Chen, X.; Wu, Z.; Liu, Y.; Hu, Z. Bi_2Te_3 Nanoplates' Selective Growth Morphology on Different Interfaces for Enhancing Thermoelectric Properties. *Cryst. Growth Des.* **2019**, 19, 7, 3639–3646. https://doi.org/10.1021/acs.cgd.8b01632.

(24) Deng, R.; Su, X.; Zheng, Z.; Liu, W.; Yan, Y.; Zhang, Q.; Dravid, V. P.; Uher, C.; Kanatzidis, M. G.; Tang, X. Thermal conductivity in $Bi_{0.5}Sb_{1.5}Te_{3+x}$ and the role of dense dislocation arrays at grain boundaries. *Sci. Adv.* **2018**, 4, 1–9. https://doi.org/10.1126/sciadv.aar5606

(25) Lee, H.; Kim, T.; Son, S. C.; Kim, J.; Kim, D.; Lee, J.; Chung, I. Unique Microstructures and

High Thermoelectric Performance in n–Type $Bi_2Te_{2.7}Se_{0.3}$ by the Dual Incorporation of Cu and Y. *Mater. Today Phys.* **2023**, *31*, 100986. https://doi.org/10.1016/j.mtphys.2023.100986.

(26) Zhu, B.; Liu, X.; Wang, Q.; Qiu, Y.; Shu, Z.; Guo, Z.; Tong, Y.; Cui, J.; Gu, M.; He, J. Realizing Record High Performance in N-Type Bi_2Te_3-Based Thermoelectric Materials. *Energy Environ. Sci.* **2020**, *13* (7), 2106–2114. https://doi.org/10.1039/d0ee01349h.

(27) Witting, I. T.; Chasapis, T. C.; Ricci, F.; Peters, M.; Heinz, N. A.; Hautier, G.; Snyder, G. J. The Thermoelectric Properties of Bismuth Telluride. *Adv. Electron. Mater.* **2019**, 5, 1800904. https://doi.org/10.1002/aelm.201800904.

(28) Mehta, R. J.; Zhang, Y.; Karthik, C.; Singh, B.; Siegel, R. W.; Borca-Tasciuc, T.; Ramanath, G. A New Class of Doped Nanobulk High-Figure-of-Merit Thermoelectrics by Scalable Bottom-up Assembly. *Nat. Mater.* **2012**, *11* (3), 233–240. https://doi.org/10.1038/nmat3213.

(29) Chauhan, N. S.; Lebedev, O. I.; Kovnir, K.; Pyrlin, S. V.; Marques, L. S. A.; Ramos, M. M. D.; Korgel, B. A.; Kolen'Ko, Y. V. Scalable Colloidal Synthesis of $Bi_2Te_{2.7}Se_{0.3}$ plate-like Particles Give Access to a High-Performing n-Type Thermoelectric Material for Low Temperature Application. *Nanoscale Adv.* **2020**, *2* (12), 5699–5709. https://doi.org/10.1039/d0na00691b.

(30) Poudel, B.; Hao, Q.; Ma, Y.; Lan, Y.; Minnich, A.; Yu, B.; Yan, X.; Wang, D.; Muto, A.; Vashaee, D.; Chen, X.; Liu, J.; Dresselhaus, M. S.; Chen, G.; Ren, Z. High-Thermoelectric Performance of Nanostructured Bismuth Antimony Telluride Bulk Alloys. *Science* **2008**, 634-638. https://doi.org/10.1126/science.1156446.

(31) Son, J. S.; Choi, M. K.; Han, M. K.; Park, K.; Kim, J. Y.; Lim, S. J.; Oh, M.; Kuk, Y.; Park, C.; Kim, S. J.; Hyeon, T. N-Type Nanostructured Thermoelectric Materials Prepared from Chemically Synthesized Ultrathin Bi_2Te_3 Nanoplates. *Nano Lett.* **2012**, *12* (2), 640–647. https://doi.org/10.1021/nl203389x.

(32) Ju, Z.; Crawford, C.; Adamczyk, J.; Toberer, E. S.; Kauzlarich, S. M. Study of the Thermoelectric Properties of Bi_2Te_3/Sb_2Te_3 Core-Shell Heterojunction Nanostructures. *ACS Appl. Mater. Interfaces* **2022**, *14* (21), 24886–24896.

https://doi.org/10.1021/acsami.2c03011.

(33) Yu, H.; Wang, D.; Han, M. Y. Top-down Solid-Phase Fabrication of Nanoporous Cadmium Oxide Architectures. *J. Am. Chem. Soc.* **2007**, *129* (8), 2333–2337. https://doi.org/10.1021/ja066884p.

(34) Jacobse, P. H.; McCurdy, R. D.; Jiang, J.; Rizzo, D. J.; Veber, G.; Butler, P.; Zuzak, R.; Louie, S. G.; Fischer, F. R.; Crommie, M. F. Bottom-up Assembly of Nanoporous Graphene with Emergent Electronic States. *J. Am. Chem. Soc.* **2020**, *142* (31), 13507–13514. https://doi.org/10.1021/jacs.0c05235.

(35) Tan, F.; Han, S.; Peng, D.; Wang, H.; Yang, J.; Zhao, P.; Ye, X.; Dong, X.; Zheng, Y.; Zheng, N.; Gong, L.; Liang, C.; Frese, N.; Gölzhäuser, A.; Qi, H.; Chen, S.; Liu, W.; Zheng, Z. Nanoporous and Highly Thermal Conductive Thin Film of Single-Crystal Covalent Organic Frameworks Ribbons. *J. Am. Chem. Soc.* **2021**, *143* (10), 3927–3933. https://doi.org/10.1021/jacs.0c13458.

(36) He, P.; Wu, Y. Constructing of Highly Porous Thermoelectric Structures with Improved Thermoelectric Performance. *Nano Res.* **2021**, *14* (10), 3608–3615. https://doi.org/10.1007/s12274-021-3555-0.

(37) Chang, P. H.; Bahramy, M. S.; Nagaosa, N.; Nikolić, B. K. Giant Thermoelectric Effect in Graphene-Based Topological Insulators with Heavy Adatoms and Nanopores. *Nano Lett.* **2014**, *14* (7), 3779–3784. https://doi.org/10.1021/nl500755m.

(38) Tang, J.; Wang, H. T.; Lee, D. H.; Fardy, M.; Huo, Z.; Russell, T. P.; Yang, P. Holey Silicon as an Efficient Thermoelectric Material. *Nano Lett.* **2010**, *10* (10), 4279–4283. https://doi.org/10.1021/nl102931z.

(39) Chen, J.; Sun, Q.; Bao, D.; Liu, T.; Liu, W. Di; Liu, C.; Tang, J.; Zhou, D.; Yang, L.; Chen, Z. G. Hierarchical Structures Advance Thermoelectric Properties of Porous N-Type β-Ag_2Se. *ACS Appl. Mater. Interfaces* **2020**, *12* (46), 51523–51529. https://doi.org/10.1021/acsami.0c15341.

(40) Wang, Y.; Liu, W. Di; Gao, H.; Wang, L. J.; Li, M.; Shi, X. L.; Hong, M.; Wang, H.; Zou, J.; Chen, Z. G. High Porosity in Nanostructured N-Type Bi_2Te_3 Obtaining Ultralow Lattice Thermal Conductivity. *ACS Appl. Mater. Interfaces* **2019**, *11* (34), 31237–31244.

https://doi.org/10.1021/acsami.9b12079.

(41) Qiao, J.; Zhao, Y.; Jin, Q.; Tan, J.; Kang, S.; Qiu, J.; Tai, K. Tailoring Nanoporous Structures in Bi_2Te_3 Thin Films for Improved Thermoelectric Performance. *ACS Appl. Mater. Interfaces* **2019**, *11* (41), 38075–38083. https://doi.org/10.1021/acsami.9b13920.

(42) Xu, B.; Feng, T.; Agne, M. T.; Zhou, L.; Ruan, X.; Snyder, G. J.; Wu, Y. Highly Porous Thermoelectric Nanocomposites with Low Thermal Conductivity and High Figure of Merit from Large-Scale Solution-Synthesized $Bi_2Te_{2.5}Se_{0.5}$ Hollow Nanostructures. *Angew. Chemie - Int. Ed.* **2017**, *56* (13), 3546–3551. https://doi.org/10.1002/anie.201612041.

(43) Dun, C.; Hewitt, C. A.; Jiang, Q.; Guo, Y.; Xu, J.; Li, Y.; Li, Q.; Wang, H.; Carroll, D. L. Bi_2Te_3 Plates with Single Nanopore: The Formation of Surface Defects and Self-Repair Growth. *Chem. Mater.* **2018**, *30* (6), 1965–1970. https://doi.org/10.1021/acs.chemmater.7b04985.

(44) Hosokawa, Y.; Tomita, K.; Takashiri, M. Growth of Single-Crystalline Bi_2Te_3 Hexagonal Nanoplates with and without Single Nanopores during Temperature-Controlled Solvothermal Synthesis. *Sci. Rep.* **2019**, *9* (1), 10790. https://doi.org/10.1038/s41598-019-47356-5.

(45) Liu, Y.; Zhang, Y.; Lim, K. H.; Ibáñez, M.; Ortega, S.; Li, M.; David, J.; Martí-Sánchez, S.; Ng, K. M.; Arbiol, J.; Kovalenko, M. V.; Cadavid, D.; Cabot, A. High Thermoelectric Performance in Crystallographically Textured N-Type $Bi_2Te_{3-x}Se_x$ Produced from Asymmetric Colloidal Nanocrystals. *ACS Nano* **2018**, *12* (7), 7174–7184. https://doi.org/10.1021/acsnano.8b03099.

(46) Iwanaga, S.; Toberer, E. S.; Lalonde, A.; Snyder, G. J. A High Temperature Apparatus for Measurement of the Seebeck Coefficient. *Rev. Sci. Instrum.* **2011**, *82* (6), 063905. https://doi.org/10.1063/1.3601358.

(47) Borup, K. A.; Toberer, E. S.; Zoltan, L. D.; Nakatsukasa, G.; Errico, M.; Fleurial, J. P.; Iversen, B. B.; Snyder, G. J. Measurement of the Electrical Resistivity and Hall Coefficient at High Temperatures. *Rev. Sci. Instrum.* **2012**, *83* (12), 123902 . https://doi.org/10.1063/1.4770124.

(48) Fievet, F.; Ammar-Merah, S.; Brayner, R.; Chau, F.; Giraud, M.; Mammeri, F.; Peron, J.;

Piquemal, J. Y.; Sicard, L.; Viau, G. The Polyol Process: A Unique Method for Easy Access to Metal Nanoparticles with Tailored Sizes, Shapes and Compositions. *Chem. Soc. Rev.* **2018**, *47* (14), 5187–5233. https://doi.org/10.1039/c7cs00777a.

(49) Cheng, L.; Chen, Z.; Yang, L.; Han, G.; Xu, H.; Je, G.; Lu, G. M.; Zou, J. T - Shaped Bi_2Te_3–Te Heteronanojunctions: Epitaxial Growth, Structural Modeling, and Thermoelectric Properties. *J. Phys. Chem. C.* **2013**, 117, 24, 12458–12464. https://doi.org/10.1021/jp4041666.

(50) Wang, W.; Goebl, J.; He, L.; Aloni, S.; Hu, Y. Epitaxial Growth of Shape-Controlled Bi_2Te_3–Te Heterogeneous Nanostructures. *J. Am. Chem. Soc.* **2010**, 132, 17316–17324. https://pubs.acs.org/doi/10.1021/ja108186w

(51) Hong, M.; Chasapis, T. C.; Chen, Z. G.; Yang, L.; Kanatzidis, M. G.; Snyder, G. J.; Zou, J. N-Type $Bi_2Te_{3-x}Se_x$ Nanoplates with Enhanced Thermoelectric Efficiency Driven by Wide-Frequency Phonon Scatterings and Synergistic Carrier Scatterings. *ACS Nano* **2016**, *10* (4), 4719–4727. https://doi.org/10.1021/acsnano.6b01156.

(52) Mi, J. L.; Nørby, P.; Bremholm, M.; Iversen, B. B. Insight into Nucleation and Growth of $Bi_2Te_{3-x}Se_x$ (x = 0-2) Nanoplatelets in Hydrothermal Synthesis. *Chem. Mater.* **2017**, *29* (12), 5070–5079. https://doi.org/10.1021/acs.chemmater.6b05211.

(53) Wang, W.; Dahl, M.; Yin, Y. Hollow Nanocrystals through the Nanoscale Kirkendall Effect. *Chem. Mater.* **2013**, *25* (8), 1179–1189. https://doi.org/10.1021/cm3030928.

(54) Railsback, J. G.; Johnston-Peck, A. C.; Wang, J.; Tracy, J. B. Size-Dependent Nanoscale Kirkendall Nanoparticles. *ACS Nano* **2010**, 4, 4, 1913–1920. https://doi.org/10.1021/nn901736y.

(55) Yang, H. Q.; Miao, L.; Liu, C. Y.; Li, C.; Honda, S.; Iwamoto, Y.; Huang, R.; Tanemura, S. A Facile Surfactant-Assisted Reflux Method for the Synthesis of Single-Crystalline Sb_2Te_3 Nanostructures with Enhanced Thermoelectric Performance. *ACS Appl. Mater. Interfaces* **2015**, *7* (26), 14263–14271. https://doi.org/10.1021/acsami.5b02504.

(56) Feutelais, Y.; Legendre, B.; Rodier, N.; Agafonov, V. A Study of the Phases in the Bismuth - Tellurium System. *Mater. Res. Bull.* **1993**, *28* (6), 591–596. https://doi.org/10.1016/0025-5408(93)90055-I.

(57) Chuang, P. Y.; Su, S. H.; Chong, C. W.; Chen, Y. F.; Chou, Y. H.; Huang, J. C. A.; Chen, W. C.; Cheng, C. M.; Tsuei, K. D.; Wang, C. H.; Yang, Y. W.; Liao, Y. F.; Weng, S. C.; Lee, J. F.; Lan, Y. K.; Chang, S. L.; Lee, C. H.; Yang, C. K.; Su, H. L.; Wu, Y. C. Anti-Site Defect Effect on the Electronic Structure of a Bi_2Te_3 Topological Insulator. *RSC Adv.* **2018**, *8* (1), 423–428. https://doi.org/10.1039/c7ra08995c.

(58) Hashibon, A.; Elsässer, C. First-Principles Density Functional Theory Study of Native Point Defects in Bi_2Te_3. *Phys. Rev. B - Condens. Matter Mater. Phys.* **2011**, *84* (14), 14–16. https://doi.org/10.1103/PhysRevB.84.144117.

(59) Zobeiri, H.; Hunter, N.; Wang, R.; Wang, T.; Wang, X. Direct Characterization of Thermal Nonequilibrium between Optical and Acoustic Phonons in Graphene Paper under Photon Excitation. *Adv. Sci.* **2021**, *8* (12), 1–12. https://doi.org/10.1002/advs.202004712.

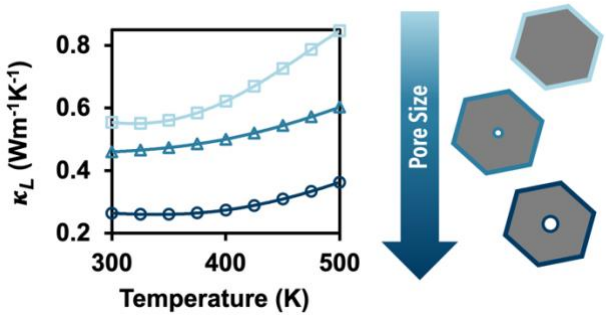

TOC